# HAL
## open science

# Modeling the Wake of the Marquesas Archipelago

H. Raapoto, E. Martinez, Anne Petrenko, Andrea M. Doglioli, C. Maes

## HAL Id: hal-01735447
## https://hal.science/hal-01735447

Submitted on 5 Jan 2022

# Modeling the Wake of the Marquesas Archipelago

**H. Raapoto[1] , E. Martinez[1] , A. Petrenko[2], A. M. Doglioli[1] , and C. Maes[3]**

[1]IRD, UPF, ILM, Ifremer, Écosystèmes Insulaires Océaniens, Tahiti, French Polynesia, [2]Aix Marseille Univ, Université de Toulon, CNRS, IRD, OSU PYTHEAS, Mediterranean Institute of Oceanography MIO, UM 110, Marseille, Cedex, France, [3]Laboratoire d 'Océanographie Physique et Spatiale, Université Brest, Ifremer, CNRS, IRD, IUEM, Brest, France

**Abstract** In this study, a high-resolution (∼2.5 km) numerical model was set up to investigate the fine-scale activity within the region of the Marquesas archipelago. This has never been performed before. The robustness of the model results is assessed by comparison with remote sensing and in situ observations. Our results highlight regions of warm waters leeward of the different islands with high eddy kinetic energy (*EKE*) on their sides. The analysis of energy conversion terms reveals contributions to *EKE* variability by wind, baroclinic, and barotropic instabilities. The use of a geometry-based eddy detection algorithm reveals the generation of cyclonic and anticyclonic eddies in the wake of the largest islands, with both an inshore and offshore effect. Maximum eddy activity occurs in austral winter following the seasonality of both wind stress and *EKE* intensity. Most eddies have a radius between 20 and 30 km and are generally cyclonic rather than anticyclonic. Significant vertical velocities are observed in the proximity of the islands, associated with topographically induced flow separation. Eddy trapping inshore waters are advected offshore in the wake of the islands. The overall influence of these fine-scale dynamics could explain the strong biological enhancement of the archipelago.

## 1. Introduction

The Marquesas archipelago (144°W–137°W; 8°S–11°S) is located in the northern part of French Polynesia, central South Pacific, where the South Equatorial Current (SEC) flows south-westward (Figure 1a). It is composed by a dozen of small volcanic islands with mountains up to 1,224 m, rugged steep cliffs, and no surrounding coral reefs (Maury et al., 2014; Figure 1b). The main five islands are Nuku Hiva (339 km$^2$), Ua Pou (105 km$^2$), and Ua Huka (83 km$^2$) in the northern part of the archipelago, and Hiva Oa (320 km$^2$) and Fatu Hiva (85 km$^2$) in the southern part. Despite their relatively small area coverage, a remarkable plume of chlorophyll-a (Chl, a proxy of phytoplankton biomass) can be observed leeward of the islands in the open ocean from satellite-derived ocean color (Martinez & Maamaatuaiahutapu, 2004; Signorini et al., 1999). Such biological enhancement is referred to as an island mass effect (IME) (Doty & Oguri, 1956). While several physical processes can be involved in the present IME, such as coastal upwelling, Ekman pumping, eddies or internal waves (Barton, 2001; Heywood et al., 1990, 1996; Palacios, 2002; Sangrà et al., 2001), the IME dominant mechanisms have not been elucidated yet for the Marquesas archipelago.

It is well known that oceanic currents encountering islands generate complex wakes. Several studies in other regions have assessed these island wakes and their forcing mechanisms using a remote sensing (DiGiacomo & Holt, 2001; Wolanksi et al., 1996), in situ data (Hasegawa et al., 2004, 2008) or a modeling approach (Dietrich et al., 1996; Dong et al., 2007; Hasegawa et al., 2009; Jiménez et al., 2008; Wolanksi et al., 1996). An important distinction has to be made between shallow-water and deep water wakes. Shallow-water wakes occur when considering islands in shallow shelves or estuaries where nearshore bottom drag acts as the primary source of vorticity generation (Alaee et al., 2004; Neill & Elliott, 2004; Wolanksi et al., 1996). Deep water wakes occur leeward tall islands surrounding by a deep bathymetry—like in the Marquesas archipelago—where bottom influence can be neglected and topographic and wind forcing are the primary sources of vorticity generation. Topographic forcing refers to the detachment of the frictional layer around the island as a result of differential bottom stress imparted to the flow by the sloping sides of the island (Dong et al., 2007). Wind forcing refers to eddy generation as a consequence of Ekman pumping induced by wind shear in the island's wake (Jiménez et al., 2008).

Eddy formation and propagation in island wakes could play a key role in the IME of the Marquesas archipelago. Indeed, a wind curl dipole has been reported in the archipelago (Martinez et al., 2009) possibly forming
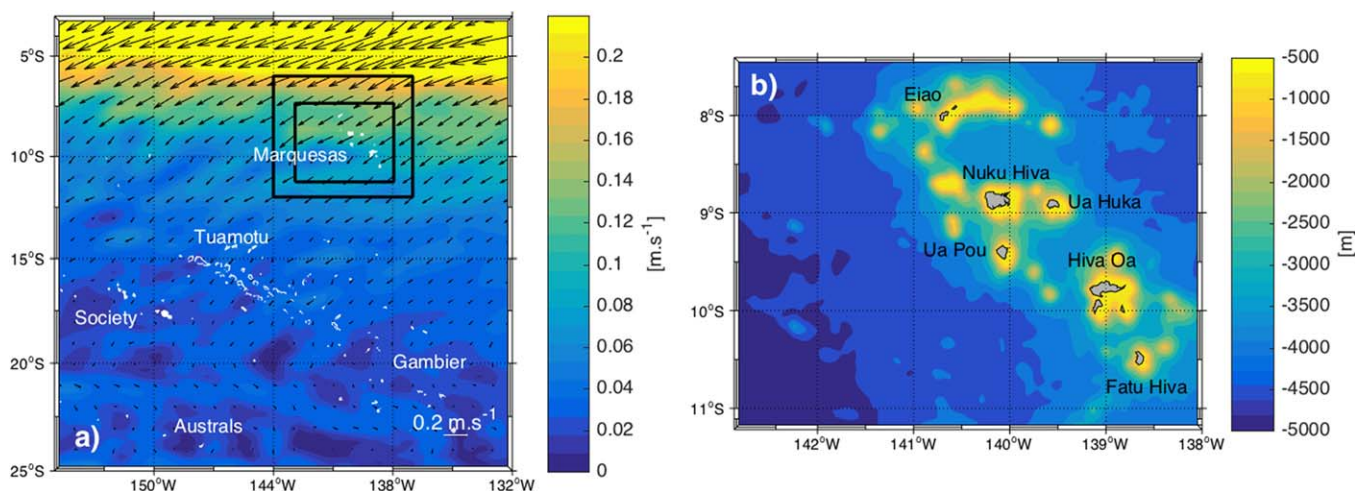
**Figure 1.** (a) Mean surface current from the satellite-derived Ocean Surface Current Analysis—Real time (OSCAR) product (time averaged over October 1992 to June 2015, in m s$^{-1}$) over French Polynesia. The islands are represented in white, as well as the name of the five archipelagos. The black boxes show the parent and child grids implemented in the ROMS configuration. (b) Bottom topography from the 2 arc min topography/bathymetry data set ETOPO2 (in m) around the archipelago used in the model configuration as well as the names of the main islands.

oceanic cyclonic eddies and jets inducing an enrichment of the upper layer leeward the islands by mechanisms such as the ones proposed by Hasegawa et al. (2009) and Andrade et al. (2014). Nevertheless, the previous studies on the Marquesas IME using satellite altimetry did not mention any eddy features (Legeckis et al., 2004; Martinez & Maamaatuaiahutapu, 2004; Signorini et al., 1999). This is probably due to the coarseness of the Sea Level Anomaly (SLA) products used in these studies. However, some eddy activity does imprint the Sea Surface Temperature (SST). For example, on 17 November 2015 (Figure 2a) a SST dipole is observed leeward Nuku Hiva at (140.5°W; 9°S), as well as a warm eddy further southwest, while a cool eddy is present at (141°W; 10.1°S) on 21 August 2012 (Figure 2b). In both cases, it is important to note that the size of the structures is of the same order than the island diameter (~30 km for Nuku Hiva). Such an eddy activity could possibly be at the origin of nutrient uplift from deep rich waters to the euphotic zone allowing the development of phytoplankton. Because the spatiotemporal resolution of satellite altimetry is too coarse to investigate the small scales of such aforementioned eddy activity around the Marquesas archipelago, recourse to high-resolution modeling taking into account the topographic forcing (i.e., the presence of the islands) has been done by the present study. Documenting the generation and characteristics of the oceanic eddies should be viewed as a first step toward an explanation of the origin of the surface layer biological enrichment in this archipelago.
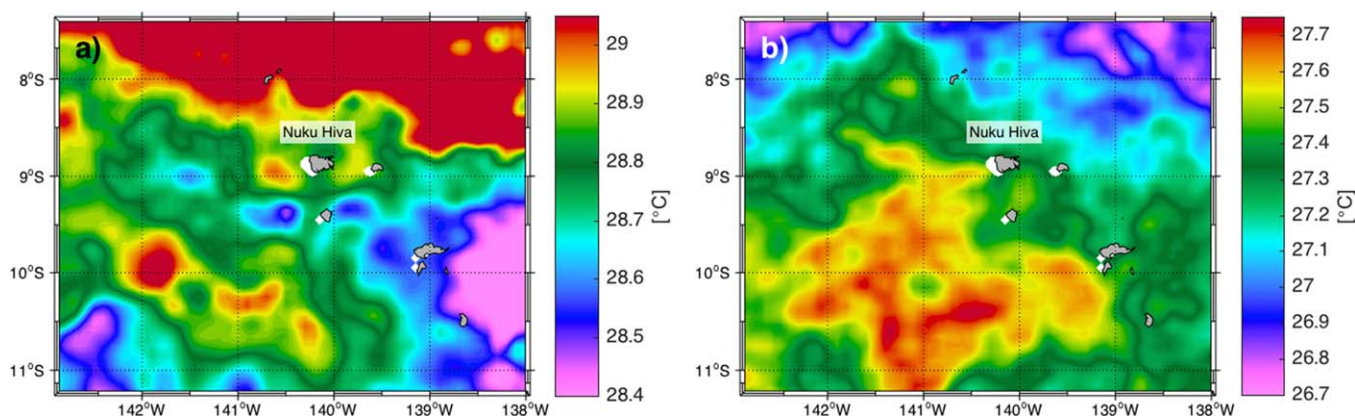


**Figure 2.** SST (°C) from Geostationary Operational Environmental Satellite (GOES)/Polar Operational Environmental Satellite (POES) in the Marquesas archipelago for (a) 17 November 2015 and (b) 21 August 2012.

The present work is organized as follows: section 2 presents the data and the methodology. A comparison of the oceanic conditions between the model, satellite and in situ observations is performed in section 3. In this section, eddy properties generated leeward the islands are also characterized. Finally, section 4 concludes this study.

## 2. Data and Methods

### 2.1. Numerical Model

Our model is based on the Regional Ocean Modeling System (ROMS)-AGRIF (Adaptive Grid Refinement in Fortran) code provided by Debreu et al. (2012) and Penven et al. (2007). The ROMS model is a split-explicit, free surface, and terrain-following vertical coordinate oceanic model (Shchepetkin & McWilliams, 2003, 2005). The AGRIF version is especially suitable to study regional scale since it has the ability to manage an arbitrary number of fixed grids and embedding levels. We configure the two-way embedding procedure. It means that the parent grid provides the boundary conditions for the child grid, and that the solution of the child grid is used to improve the larger scale parent grid solution, allowing a smooth, continuous interfacing between grid levels (Debreu & Blayo, 2008; Debreu et al., 2012). Therefore, we defined two embedded grids: (1) the parent grid extends from 137°W to 144°W and 6°S to 12°S; (2) the child grid extends from 138°W to 143°W and 7.3°S to 11.3°S as shown in Figure 1a. The grid refinement rate is 3, implying a 1/15° (∼7 km) and 1/45° (∼2.5 km) grid resolutions for the parent and child grids, respectively. This allows a sufficient sampling of the island topography and of the fine-scale dynamics, as the first baroclinic Rossby radius of deformation is about 120 km in this region according to Chelton et al. (1998). The internal (external) time stepping is set to 3,600 (600) s for the parent grid and 1,200 (200) s for the child grid. Both grids have 32 vertical levels and the vertical s-coordinate is stretched for boundary layer resolution. The topography is derived from the 2′ resolution ETOPO2 database provided by NOAA-NGDC (Smith & Sandwell, 1997). The bathymetry field has been filtered to keep the slope parameter <0.25 (Beckmann & Haidvogel, 1993). The K-profile parameterization (KPP) vertical mixing scheme from Large et al. (1994) is used to parameterize vertical mixing processes.

All the external forcings of the ROMS simulations are based on monthly climatologies. At the surface, the heat and freshwater fluxes are extracted on a monthly $1/2°$ grid from the Comprehensive Ocean-Atmosphere data set (COADS) (da Silva et al., 1994). The wind forcing is issued from the QuikSCAT monthly climatology calculated over 1999–2009, on a $1/4°$ grid (Lungu & Callahan, 2006). ROMS is connected to the lateral boundaries by an active, implicit and upstream-biased radiation condition (Marchesiello et al., 2001). The boundary conditions and initial state are based on the objectively analyzed World Ocean Atlas 2013 (WOA13) monthly climatology on a $1/4°$ grid (Locarnini et al., 2013; Zweng et al., 2013). The inflow boundary conditions are nudged toward temperature, salinity, and geostrophic velocity fields. Following Kersalé et al. (2011), the nudging time scale for inflow and outflow are set to 1 day and 1 year for the tracer fields and 3 days and 1 year for the momentum fields. The geostrophic velocity is referenced to the 1,000 m depth. The explicit lateral viscosity is null all over the domain, except in the sponge layer. The width of the nudging border is 50 km and the maximum viscosity value for the sponge layer is set to 1,000 $m^2 s^{-1}$.

The high-resolution ROMS simulation, hereafter referred to as W13Q, is run over 10 years with outputs averaged every 2 days. Integrated physical properties show that a statistical equilibrium is reached by the model after the first year of simulation. To avoid any impact of the spin up on the model output and to ensure the robustness of our findings, we decided to also entirely remove the third year and to focus our investigation on the outputs from year 4 to 10.

### 2.2. Data Sets

We compared our numerical results with several data sets. The Moderate Resolution Imaging Spectroradiometer (MODIS) infrared SST measured from the Aqua satellite are available on a monthly basis with a spatial resolution of 4 km. We use the time period from July 2002 to June 2015 to compute the monthly climatology.

The 3-D monthly fields of temperature and salinity issued from the In Situ Analysis System (ISAS13) are based on Argo data (Gaillard et al., 2016) and are available on a 0.5° grid from 2002 to 2012.

Monthly near surface current over 1992 to 2015 are obtained from the Ocean Surface Current Analysis—Real time (OSCAR) with a 1/3° spatial resolution (Bonjean & Lagerloef, 2002).

Finally we used reanalyzed currents from the global Hybrid Coordinate Ocean model and the Navy Coupled Ocean Data Assimilation (HYCOM + NCODA) (Cummings & Smedstad, 2013). These velocity fields are available with a spatial resolution of 1/12.5° and a daily resolution from 1 January 2006 to 31 December 2012.

### 2.3. Nondimensional Numbers

The ocean dynamics in island wake is generally characterized by the recourse to nondimensional numbers issued from geophysical fluid dynamics. The wake is typically controlled by the turbulent Reynolds number defined as:

$$Re = U_0 D / v$$

where $U_0$ is the unperturbed upstream velocity, $D$ is the horizontal scale of the obstacle, and $v$ is the eddy viscosity (Tomczak, 1988). To compute $Re$ in the Marquesas Islands, we use an horizontal eddy viscosity value of $v = 100$ m$^2$ s$^{-1}$ (Heywood et al., 1990; Jiménez et al., 2008). In the archipelago, only the biggest island, Nuku Hiva, exhibits a Reynolds number ($Re \approx 50$) that exceeds the theoretical threshold of the Von Karman vortex street generation ($Re_{th} = 40$).

To consider the spatial scale and energy involved in island wake, we also consider the Burger number, representing the ratio between stratification and Earth's rotation, and defined as:

$$Bu = \left(\frac{R_d}{R}\right)^2$$

where $R$ is the island radius and $R_d$ the Rossby radius associated to the first baroclinic mode. Using the forcing data from WOA13, we found that the seasonality of $R_d$ vary between 120 and 130 km in the archipelago. When the island radius $R$ is smaller than $R_d$ ($Bu \geq 1$), a submesoscale wake is generated with eddies having their radius in the order of $R$ (Stegner, 2014). This is always the case in the archipelago where the radius of the largest island is about 20 km.

Finally, we calculate the geometric shallow-water parameter $\alpha = \frac{h}{R}$, with $h$ the mean thermocline depth. We obtained an alpha ranging between 0.01 and 0.03. These values are typical of mid-ocean isolated islands, such as Madeira (Caldeira et al., 2002), Gran Canaria (Sangrà et al., 2005) or Hawaii (Calil et al., 2008), generating a deep water wake.

### 2.4. Eddy Detection and Tracking

To detect eddies in our model experiment, the method based on the geometry of the flow field developed by Nencioli et al. (2010) is applied. This method is well established and used in several studies with different resolution (Amores et al., 2013; Dong et al., 2012; Liu et al., 2012; Mkhinini et al., 2014). It relies on the spatial definition of vortices defined as a region with a rotary flow around its center. In other words, a vortex is defined as a region with velocity vectors rotating around a center with a minimum speed. Its boundary is defined by the largest closed contour line of the local stream function around the center. The flexibility of the algorithm depends on two parameters: $a$, the number of grid points where the current increases, and $b$, the dimension of the area used to define the local minimum of velocity. These parameters set the minimum size of the detectable vortices and allow the algorithm to work on different grid resolution. Using the same protocol than Nencioli et al. (2010) and Liu et al. (2012), optimal performances of the algorithm have been obtained with $a = 2$; $b = 2$ for our model configuration and $a = 3$; $b = 2$ for the HYCOM reanalysis outputs.

Once eddies have been detected at each time step, we used the tracking method proposed by Doglioli et al. (2007) and Nencioli et al. (2010): the position and sign of each eddy center are compared at successive time steps. An eddy track is identified when the eddy center at the next time step is found within a given searching area of the previous time step. The searching radius is the product of the averaged eddy center displacement speed and the time interval between two model outputs (i.e., 2 days). To avoid that eddies move further than the searching area within successive time steps (thus preventing track splitting), we added a constant of 20 cm s$^{-1}$ corresponding to the eddy-center displacement speed and representing the mean velocity of the background current. Moreover, eddies with a shorter lifetime than 4 days are not considered to ensure the only detection of consistent structures only.

The data set obtained after applying the detection includes: eddy-center locations, eddy contours, polarities, and radii. Time evolution of each eddy detected is also recorded and gives us information on their generation and ending.

### 2.5. Eddy Kinetic Energy Budgets

The *EKE* is defined as the kinetic energy due to transient dynamic. Neglecting the vertical velocity contributions: $EKE = \frac{1}{2}\left(u'^2 + v'^2\right)$, where $u' = u - \overline{u}$ and $v' = v - \overline{v}$, with $u$ and $v$ the zonal and meridian components of the velocity at 10 m, $\overline{u}$ and $\overline{v}$ their temporal means from year 4 to 10. To consistently compare our numerical model results with the monthly satellite-derived observations (OSCAR), we subsampled the W13Q current components at 10 m ($u_m$ and $v_m$) by extracting one grid point every five grid points. Then, we used monthly averages to compute the monthly $EKE_m = \frac{1}{2}\left(u_m'^2 + v_m'^2\right)$.

To quantify the relative importance of instability and eddy-mean interaction mechanisms on the *EKE* generation, we consider the different terms of energy budgets relative to the *EKE* generation (Auad et al., 1991; Liang et al., 2012; Marchesiello et al., 2003). The wind work, the barotropic and the baroclinic energy conversion (Dong et al., 2007; Halo et al., 2014; Hristova et al., 2014; Sun et al., 2016) are defined, respectively, as:

$$FeKe = -\frac{1}{\rho_0}\left(\overline{u'\tau_x'} + \overline{v'\tau_y'}\right)$$

$$KmKe = -\left(\overline{u'u'}\frac{\partial \overline{u}}{\partial x} + \overline{u'v'}\frac{\partial \overline{u}}{\partial y} + \overline{u'w'}\frac{\partial \overline{u}}{\partial z} + \overline{v'u'}\frac{\partial \overline{v}}{\partial x} + \overline{v'v'}\frac{\partial \overline{v}}{\partial y} + \overline{v'w'}\frac{\partial \overline{v}}{\partial z}\right)$$

$$PeKe = -\frac{g}{\rho_0}\overline{\rho'w'}$$

where $\tau_x$ and $\tau_y$ are the meridian and zonal component of the wind stress. The prime indicates the anomaly from the annual mean. $g$ is the gravity, $\rho$ is the density and $\rho_0 = 1{,}030$ kg m$^{-3}$. The overbar denotes the temporal mean and the prime represents the anomaly deviation from the mean. The *FeKe* is the *EKE* generation due to transient wind. When positive, this term induces an energy input while, when negative, it implies a damping effect on the sea surface (Xu & Scott, 2008). The *KmKe* is the energy conversion between mean currents and *EKE*. When its volume-integration is positive, it implies barotropic energy conversion. The *PeKe* is the energy conversion between available potential energy and *EKE* and indicates baroclinic instability when its volume-integration is positive (Harrison & Robinson, 1978). Both *KmKe* and *PeKe* are vertically integrated over the surface layer (top 100 m) (Hristova et al., 2014). The minimum depth in the model is set to 75 m. When the bathymetry is shallower than 100 m, conversion terms are integrated over the actual depth.

## 3. Results and Discussion

### 3.1. Thermohaline Structures and Seasonal Variability

The Marquesas archipelago is characterized by a north-east/south-west SST gradient as shown by MODIS remote sensing data and W13Q (Figures 3a and 3b). Colder water in the north-east ($\leq 27.5°C$) represents the imprint of the equatorial upwelling (Wyrtki, 1981) while warmer SST in the west ($\geq 28°C$) is the southeastward imprint of the western Pacific warm pool (Yan et al., 1992). The high-resolution of MODIS reveals warm regions behind the islands likely due to areas zones of weak currents leeward the islands. These structures have also been observed leeward several islands elsewhere (Caldeira et al., 2002; Caldeira & Marchesiello, 2002). The maximum of the mean satellite SST over the archipelago is up to 28.6°C in April during the austral summer (Figure 3c, black line). In austral winter (September), SST in the Marquesas region decreases down to 27°C. In this tropical region, the seasonal amplitude is around 2°C as confirmed by in situ SST from ISAS13 (red line). All the aforementioned features appear in the same locations and with comparable amplitudes in our numerical experiment, although SST is slightly colder than satellite observations (0.05–0.1°C; Figure 3b versus 3a; green line in Figure 3c). Thus, SST seasonal climatology from the model shows a good agreement with in situ and satellite-derived temperature variability.

Considering the haline structure, in situ data from ISAS13 show a SSS maximum in austral summer and a minimum in austral winter (35.7 and 35.5 psu ± 0.01 psu), that are satisfactory reproduced by the model (Figure 4a). The TS diagram issued from ISAS13 and W13Q illustrates the water masses within the
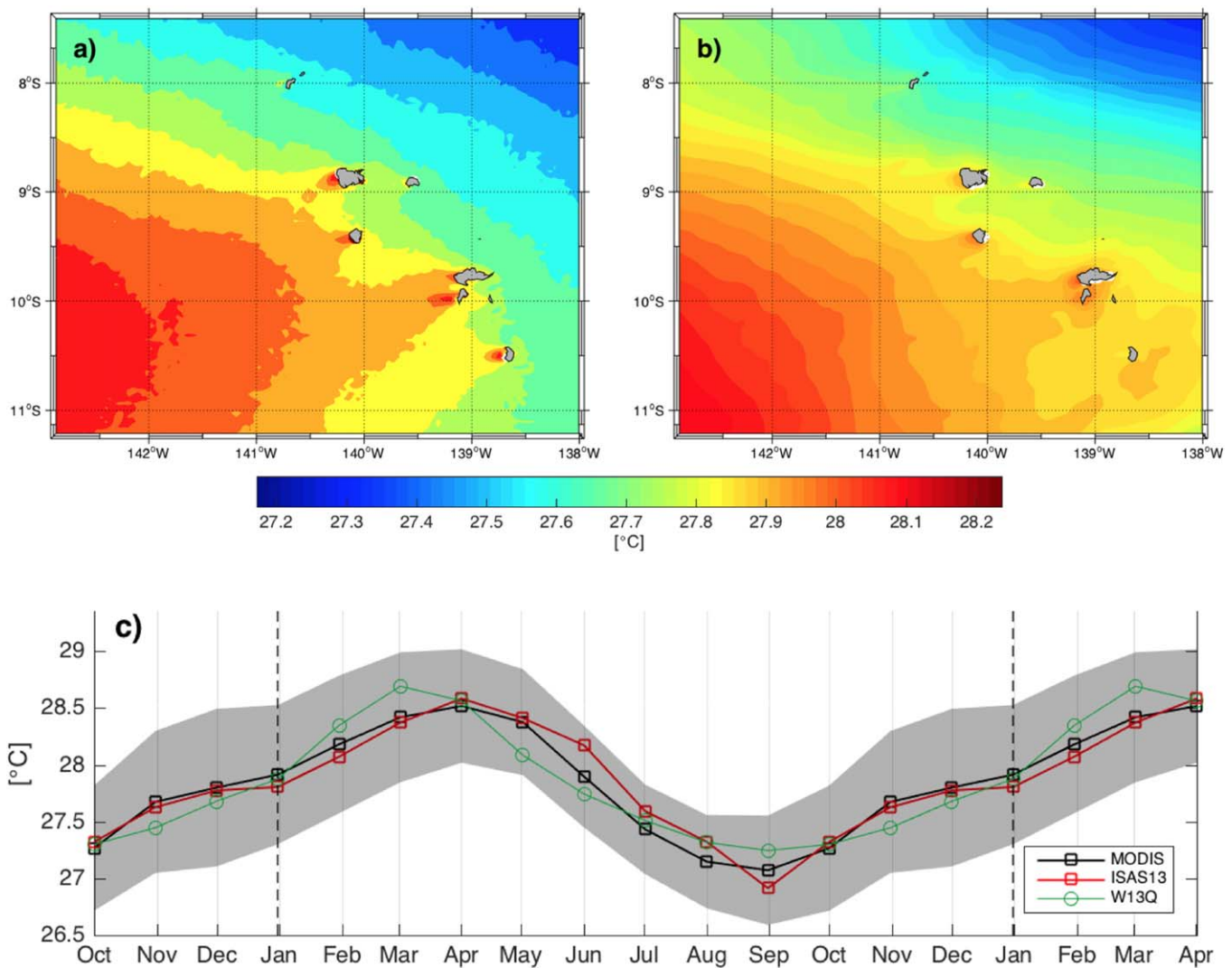
**Figure 3.** Mean SST over the child grid area from (a) MODIS (time averaged from July 2002 to June 2015) and (b) W13Q at 10m (time averaged over year 4–10). (c) Monthly climatology averaged over the child grid area from MODIS (black), ISAS13 (red), and W13Q (green). The gray shaded area represents the spatial standard deviation from MODIS monthly climatology. Units are in °C.

archipelago (Figure 4b). The South Pacific Tropical Water (SPTW) is characterized by a salinity maximum in subsurface (>35.6 psu) (O'Connor et al., 2005). The Eastern South Pacific Central Water (ESPCW) and the Antarctic Intermediate Water (AAIW) are, respectively, defined by temperature ranges between 8 and 24°C and between 2 and 10°C. Their salinities are ranging between 34.4 psu and 36.4 psu and between 33.8 psu and 34.5 psu, respectively (Emery, 2001). Only the SPTW is fresher in W13Q than with in situ measurements. The other water masses are quite well reproduced.

### 3.2. Current Structures

As shown in Figure 1a, the SEC is the main surface current flowing around the Marquesas archipelago. Currents issued from W13Q present the same order of magnitude than the OSCAR ones, although with a more westward direction in the north (Figure 5a). The spatial distribution of the mean current in the archipelago can be depicted in two regions: the southern part where the horizontal current is weak (8 cm s$^{-1}$), and the northern part where the SEC is stronger and reaches values of 20 cm s$^{-1}$ as observed by Martinez et al. (2009). The deviation of the SEC creates stronger currents on both sides of the islands and regions of weak current just behind the islands (Figure 5b) (Chang et al., 2013; Karnauskas et al., 2017). These shadow zones of weak currents are collocated with the warm areas as reported previously in Figure 3b.
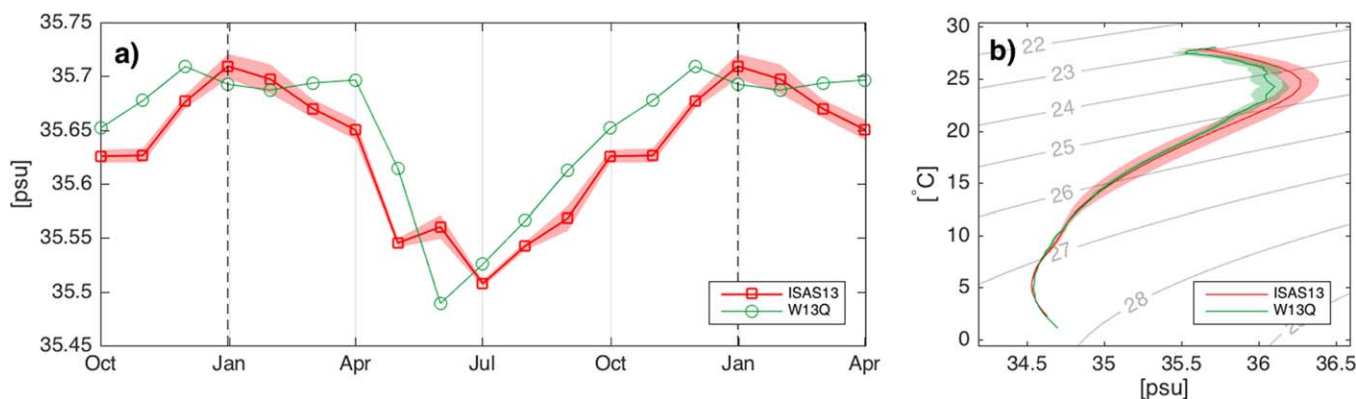
**Figure 4.** (a) Time series of the monthly averaged salinity (in psu) at 10 m issued from ISAS13 (red) and W13Q (green). Red shaded area corresponds to the spatial standard deviation from ISAS13. (b) TS diagram from ISAS13 (red) and W13Q (green) monthly climatology and their standard deviations (red and green shades, respectively).

### 3.3. *EKE* Generation and Seasonal Variability

In order to investigate the dynamical properties within the archipelago and more precisely the eddy field, we first focus on the *EKE* characterization. The $EKE_m$ obtained from OSCAR monthly currents show homogeneously low values around the archipelago (25 cm$^2$ s$^{-2}$) in Figure 6a. In the northern and the south-western part of the archipelago, two areas are barely more active, the former corresponding to the southward imprint of the turbulent equatorial area (Qiu & Chen, 2004). To compare the eddy activity from W13Q with the remote sensed one, we subsampled the model outputs to the same spatial and temporal resolution before computing $EKE_m$ (Figure 6b). High activity occurs in the northern and south-western part of the archipelago. Monthly W13Q also presents a high eddy activity west of Nuku Hiva. To fully take advantage of the high-resolution model, the annual mean of *EKE* is now directly computed from the W13Q 2-day outputs (Figure 6c). Thanks to the higher spatial and temporal resolution, the *EKE* at 10 m reaches up to 90 cm$^2$ s$^{-2}$ (versus 55 cm$^2$ s$^{-2}$ in Figure 6b). Island wakes characterized by a highly variable *EKE* pattern are highlighted westward the northern islands of Nuku Hiva, Ua Pou, and Ua Huka. We could have also expected high activity leeward Hiva Oa (in the south), since its diameter is approximately the same as Nuku Hiva. However, the
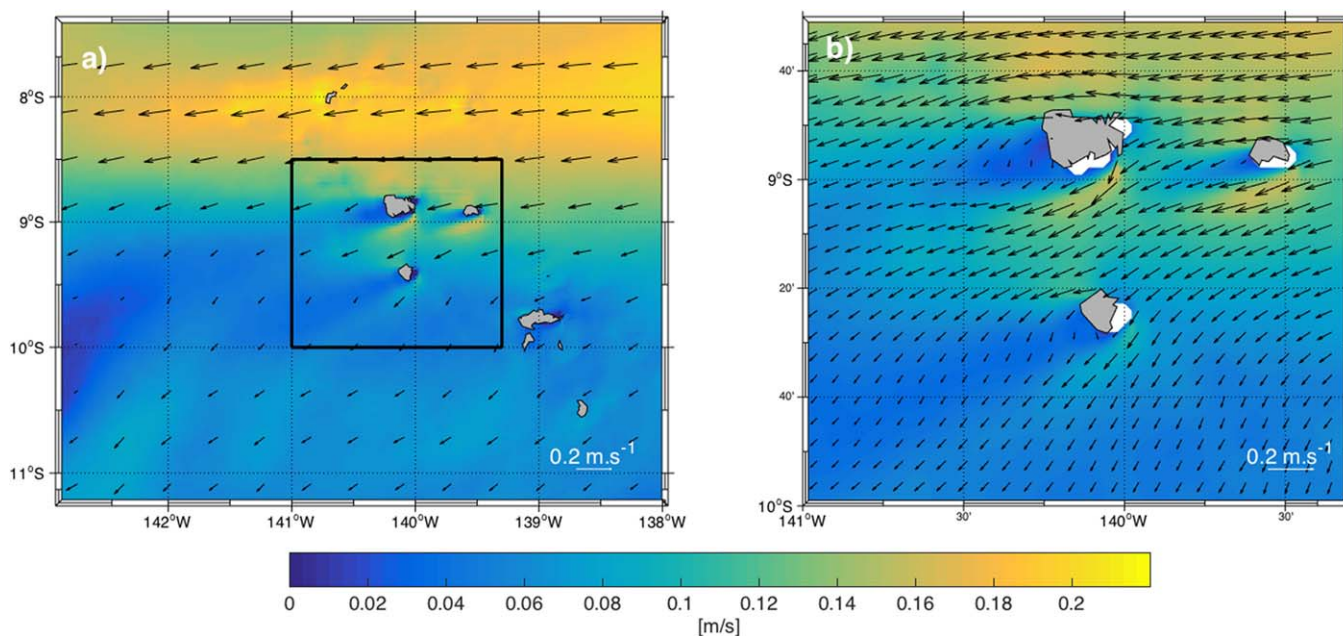


**Figure 5.** (a) W13Q current at 10 m time averaged over year 4–10 and over the child domain. For clarity, only 1 vector each 17 is represented. (b) Zoom of (a) over the Marquesas northern islands, as defined by the black box on a). For clarity, only 1 vector each 3 is represented. Units are in m s$^{-1}$.
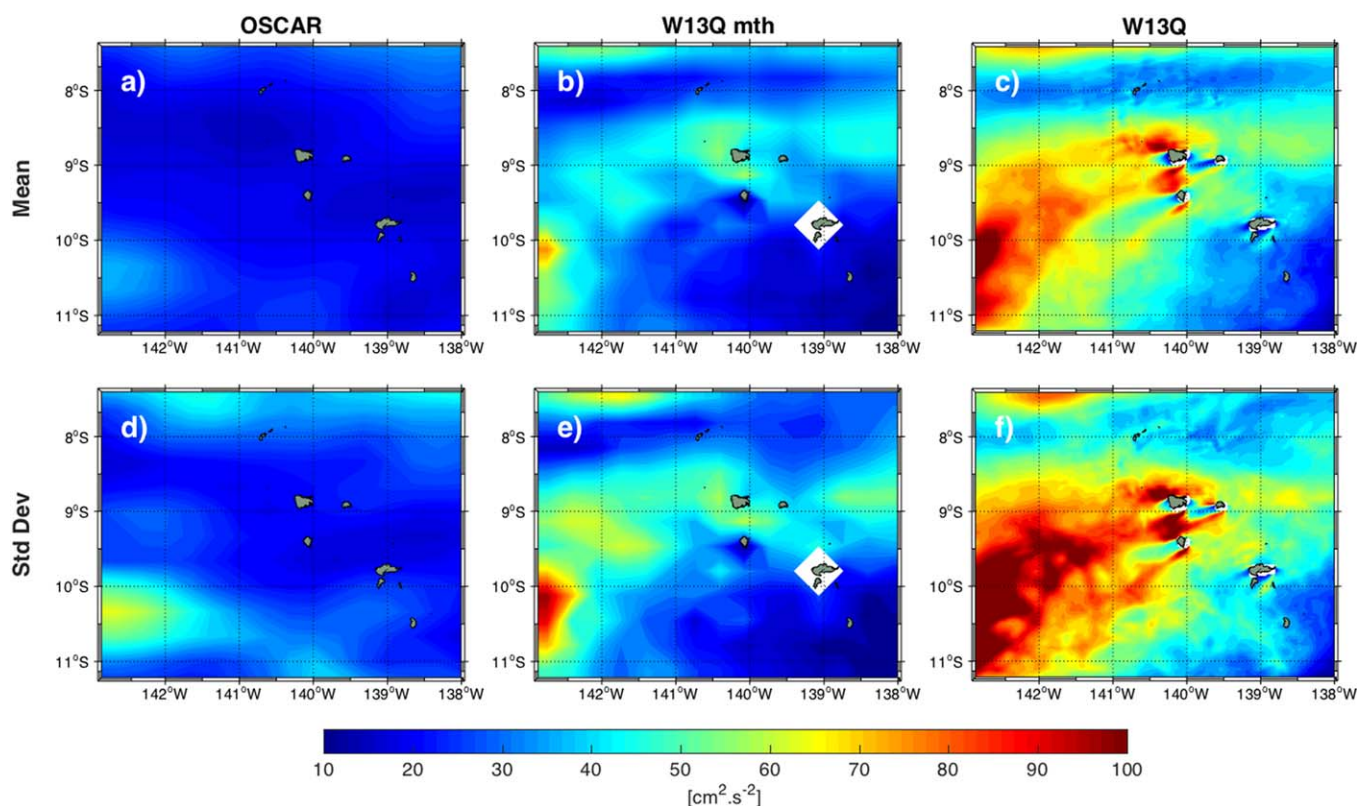
**Figure 6.** Annual mean of $EKE_m$ (in $cm^2 s^{-2}$) obtained from monthly averaged of (a) OSCAR surface currents and (b) W13Q currents at 10 m. (c) The annual mean of $EKE$ derived from the W13Q 2 day outputs. Their standard deviations are represented in Figures 6d–6f, respectively. Blanking in panels b and e are due to the subsampling.

SEC being weaker windward this island, it does not produce a strong enough $EKE$. Consistently, $EKE$ patterns are more pronounced in the northern part of the archipelago where the mean current is stronger as seen on Figure 5a. The $EKE$ standard deviations are given in Figures 6e and 6f. They reveal high activity where the mean $EKE$ is already high and in good agreement with OSCAR $EKE$ standard deviations (Figure 6d).

In order to determinate the $EKE$ origin, we now investigate the energy budget. For all the islands, the Burger number $Bu > 1$. Therefore, a significant amount of kinetic energy in the $EKE$ origin is expected. This trend is observed in the barotropic energy conversion (Figure 7a). The $KmKe$ is particularly intense leeward Nuku Hiva where the $EKE$ pattern is the strongest (Figure 6c). It is mainly due to the fact that Nuku Hiva is the largest island and that it lies where the currents are the strongest. This implies a Re = 58 and, consequently, a possible Von Karman wake generation. $KmKe$ and $PeKe$ spatial patterns are close and are driven by the topography of the archipelago (Figures 7a, 7b, and 1b). The distribution of the baroclinic energy conversion is negative in average, which indicates an eddy dissipation toward the eddy potential energy (Kang & Curchitser, 2015). The averaged energy input from the wind ($FeKe$) presents smooth patterns because of the relatively low resolution of the wind stress used in the model (Figure 7c). Values are weaker than the two previous parameters.

The $EKE$ seasonality is superimposed with the different energy budget terms and their sum in Figure 7d. $EKE$ time series show a maximum activity in February, June and August, when the $KmKe$ is also high. The latter remains positive all year round, indicating a constant flux toward $EKE$. $PeKe$, in a smaller proportion, also contributes to the high $EKE$ activity in February. $PeKe$ is responsible for the minimum value of $EKE$ in April. The $EKE$ variation on the second half of the year is explained by the $FeKe$ variation, with a decreasing activity from August to December. The sum of these energy flux terms is relatively well correlated with the $EKE$ variability. When this sum is positive (negative), an increase (decrease) of $EKE$ is observed except during June where the energy budget seems too low to explain the $EKE$ activity. According to Chen et al. (2016), residual terms of energy in the energy transfer through eddy-mean flow interactions could be imbalanced and
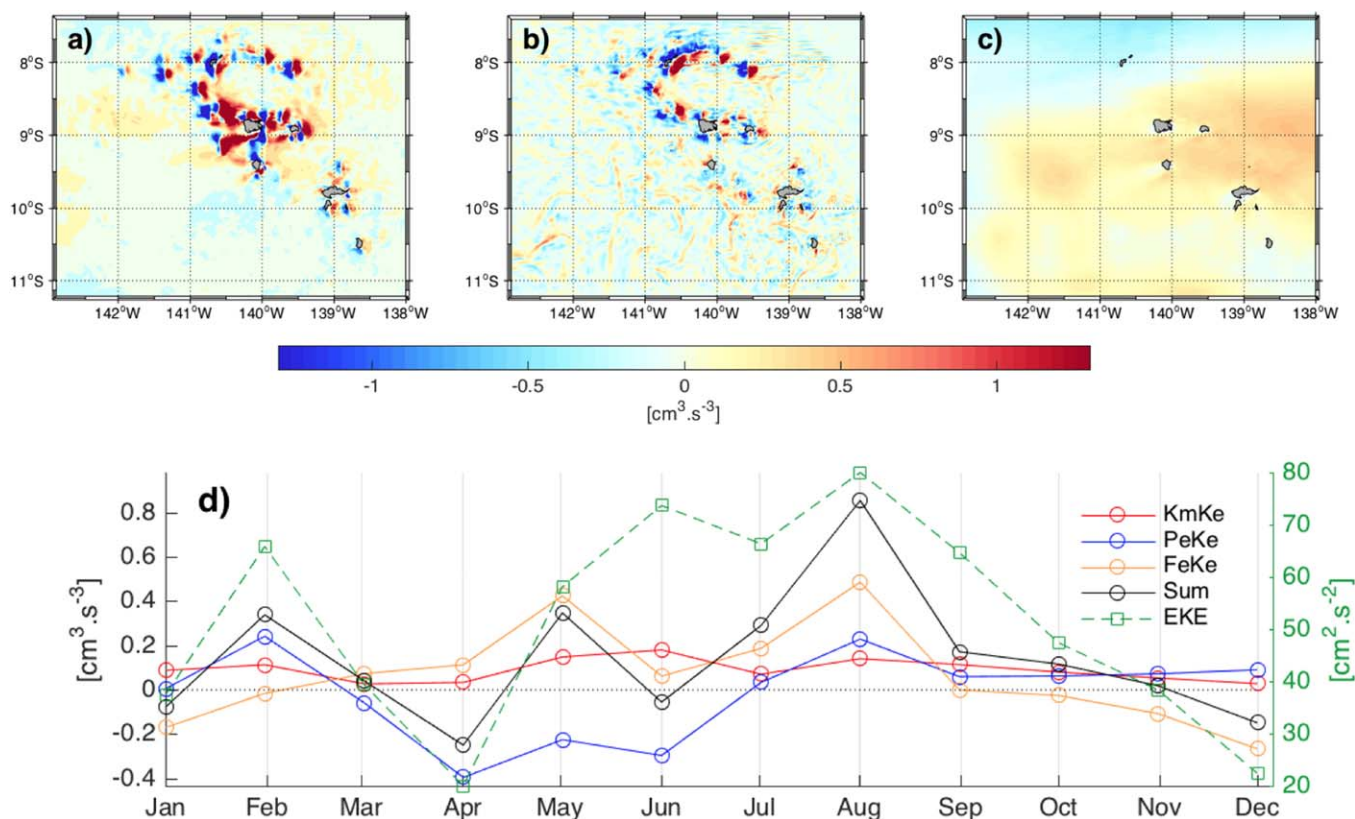
**Figure 7.** Spatial distribution of the annual mean of the the (a) barotropic (*KmKe*), (b) baroclinic (*PeKe*) energy conversion both integrated over the surface to 100 m, and (c) the *EKE* generation due to transient wind, from year 4 to 10 of W13Q (units are in cm³ s⁻³). (d) Time series of wind work, baroclinic and barotropic energy (left axis), in yellow, blue and red, respectively. The sum of these three terms is indicated in black. The *EKE* (in cm² s⁻², right axis) spatially averaged over the child grid and at 10 m is represented in green.

compensated by advection. Indeed, currents are relatively intense in the archipelago during this time period. This could be at the origin of the decay observed in these time series. Although the spatial averaging reveals low values of *PeKe* and *FeKe* compared to some local maxima (Figures 7a and 7b), these energy inputs seem to play an important role in the *EKE* seasonal variation, particularly at the beginning and the end of the year.

### 3.4. Eddy Activity

Detected eddies within the Marquesas archipelago are illustrated with green contours on relative vorticity maps from 22 June to 22 July during year 9 of W13Q (Figure 8). Positive (negative) values reveal anticyclonic (cyclonic) circulation. The total number of detected eddies over the 7 years of integration is 1,260, with a dominance of cyclonic (714) versus anticyclonic eddies (546). This cyclonic eddy dominance (i.e., 56.7% of the total eddy number) is well illustrated (Figure 8). On the other hand, positive patterns are unstable and tend to broaden and fragment inducing a weaker proportion of anticyclonic eddies. These observations are consistent with previous studies and are due to centrifugal instability occurring to anticyclonic eddies (Dong et al., 2007; Hasegawa et al., 2009; Stegner, 2014). These snapshots reveal an important eddy activity in the archipelago which has never been investigated before. In particular, Figure 8c shows the generation of cyclonic and anticyclonic eddies leeward Nuku Hiva, the northern island, and likely producing SST small-scale patterns as observed in Figure 2.

To investigate where eddies are generated, the first eddy position determined by the detection algorithm is recorded and analyzed. Most of eddies are generated leeward the archipelago highlighting the role of the topography (Figure 9a). Part of these eddies are generated just behind the islands. Although the mean Reynolds number is larger than 40 only for Nuku Hiva, eddies are also generated behind the other islands. Indeed, when surface currents accelerate on the flanks of the other islands (Figure 5), they induce a larger
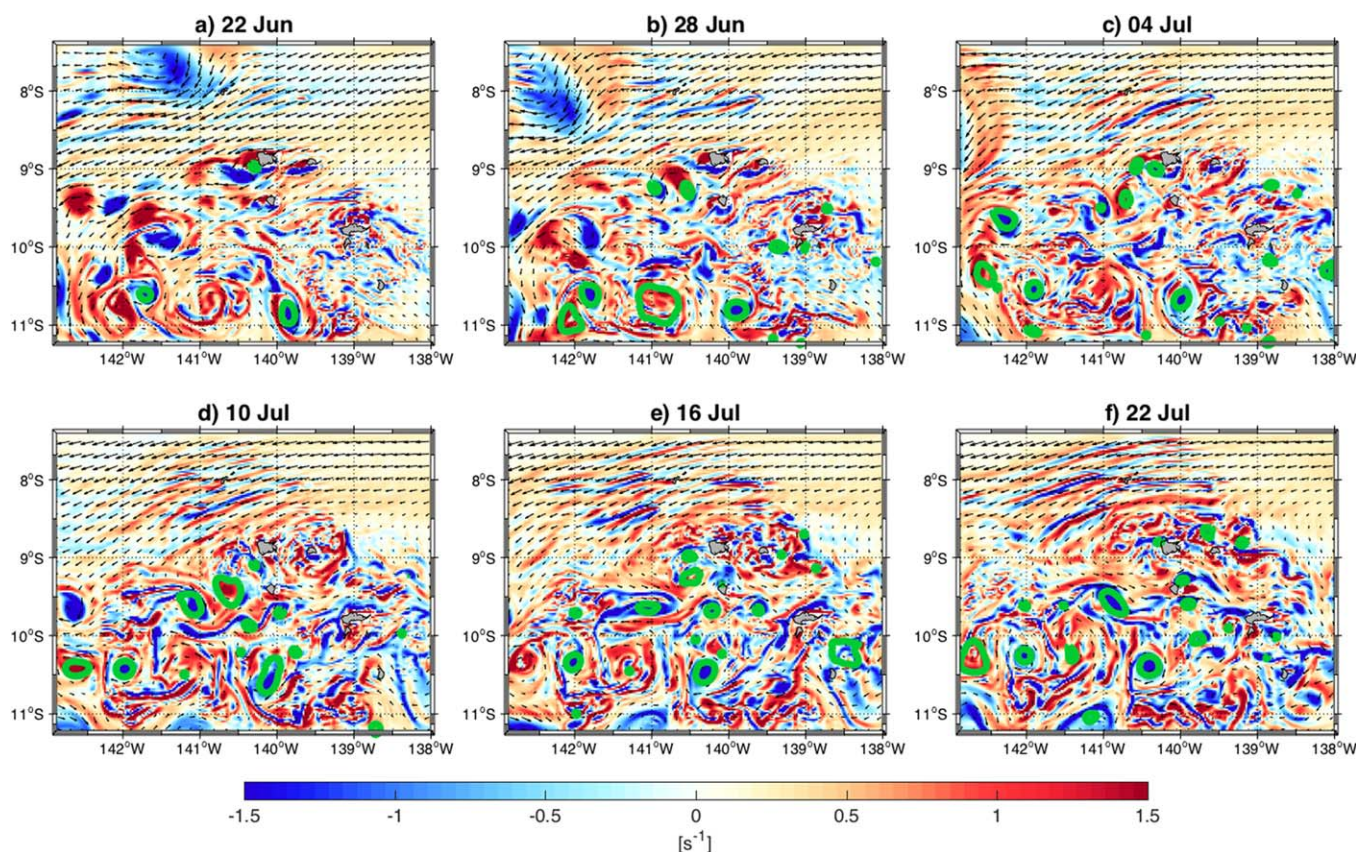
**Figure 8.** (a–f) Snapshots of relative vorticity at 10 m (units are in $s^{-1}$) from W13Q during Year 9 every 6 days. The detected eddies are represented by *green* contours (Nencioli et al., 2010 based algorithm). The animation of the vorticity from June to July is available in the auxiliary material.

Re and create a decreasing pressure in the lee side associated with two opposite recirculation cells behind the islands. Anticyclonic eddies are generated on the equatorward side and cyclonic eddies on the poleward side. These eddies are emphasized behind Nuku Hiva and Ua Pou in the northern part of the archipelago where the SEC is the strongest, and Hiva Oa in the south which is the second biggest island of the Marquesas archipelago. Conversely, there is no eddy generation behind Ua Huka (the northeastern most island) due to its small size inducing a too low Re (=34) while there is a signature of the island wake on *EKE* (Figure 6c), mean currents (Figure 5), energy conversion rates (Figure 7a), and vorticity (Figure 8).

Eddies are also generated farther from the coasts, in the open ocean, where the flow presents complex structures as seen in Figure 8. They are generated almost exclusively south-westward of the islands. A small number is also generated elsewhere, likely due to an eastward perturbation of the SEC during austral winter and referred as the Marquesas Counter Current (Martinez et al., 2009). Most of the eddies in the archipelago are generated during austral winter (July and August) when the wind stress and the *EKE* are maximum (Figures 9b and 7c). Contrarily, eddies are barely detected in March and April when the wind stress and *EKE* are minimum. A strong correlation is found between eddy generation and the wind stress, with $r=0.87$ ($p=2 \times 10^{-4}$). A high eddy generation occurs when the wind is strong (Figure 9b). Indeed, not only the wind is responsible for a part of the *EKE* generation, but it also strengthens the surface currents, providing sufficient velocity to generate eddies behind the islands.

Investigating the maximum size of the detected eddies during their lifetime in W13Q shows that their distribution is similar to a Gaussian without an inferior tail due to resolution limitations (Figure 10a, green bars). Most of the eddy radii are lower than 25 km and only a few are larger than 45 km. Indeed, size of eddies generated leeward the islands are approximately the same than the island dimensions, which can be explained by *Bu* larger than 1. The HYCOM eddy size distribution from January 2006 to December 2012 has been investigated within the child grid (Figure 10a, black bars). In opposition with the W13Q results, a
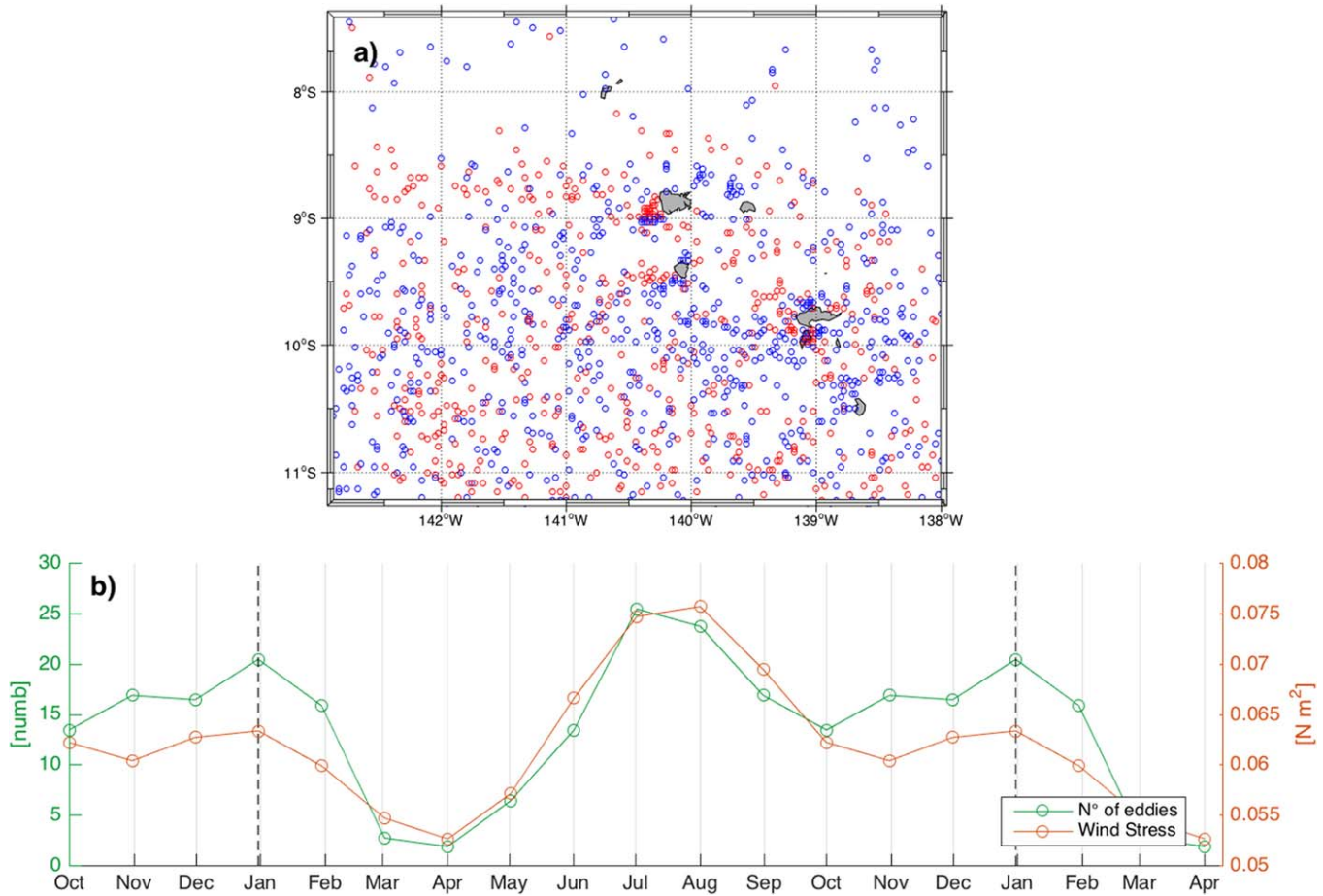
**Figure 9.** (a) Location of eddy generation identified from W13Q over year 4 to 10. Anticyclonic and cyclonic eddies are represented by red and blue circles, respectively. (b) Monthly mean number of generated eddies from W13Q from year 4 to 10 (green line) and wind stress issued from QuickSCAT in N m$^{-2}$ (orange line).

significant number of eddies larger than 20 km is present while smaller eddies are absent in HYCOM. The coarser spatial resolution of HYCOM prevents the resolution of such small structures. HYCOM larger eddies are suspected to be induced by the interannual forcing which is not represented in the present climatological W13Q configuration. In total, almost three times more eddies, are detected in our configuration than in HYCOM resulting from the higher resolution of our model.
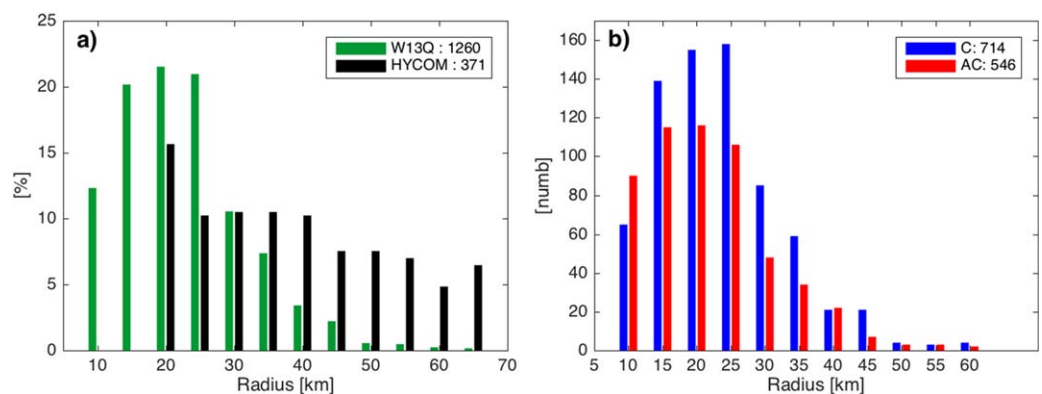


**Figure 10.** (a) Distribution of the detected eddy radius from year 4 to 10 in W13Q (green) and from 2006 to 2012 in HYCOM (black). (b) Distribution of W13Q cyclonic (blue) versus anticyclonic (red) eddies.
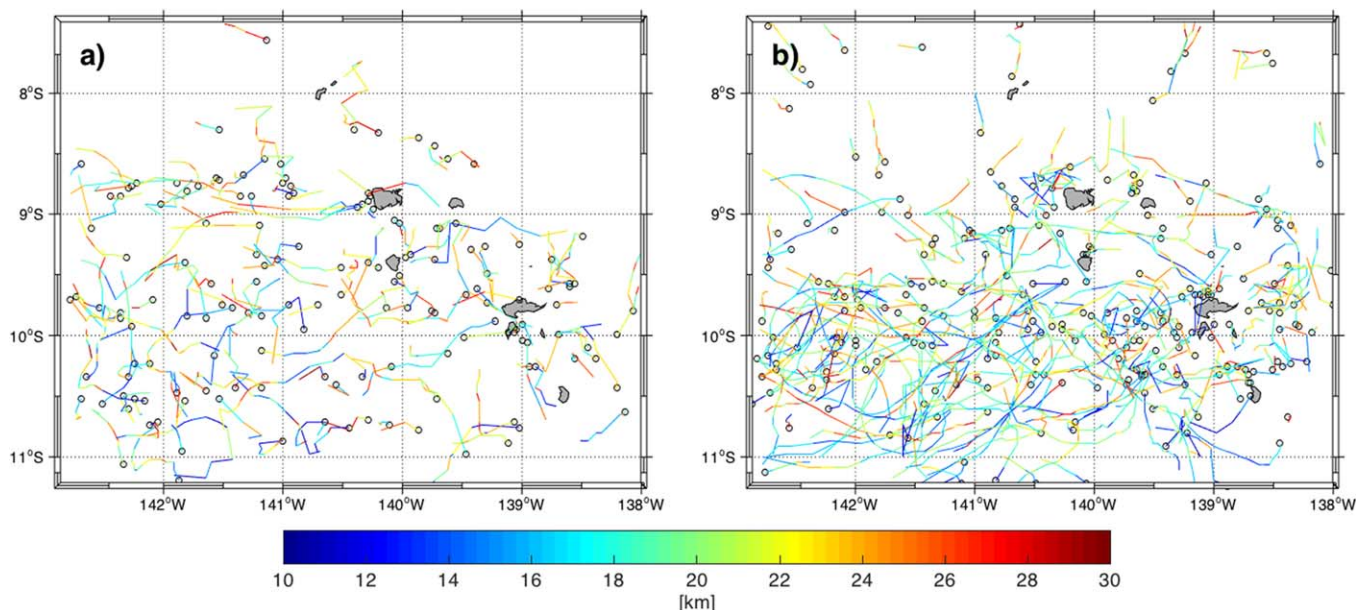
**Figure 11.** Eddy generation sites (black circles) and their trajectories for (a) anticyclonic and (b) cyclonic eddies detected in W13Q and for a maximum radius over 20–30 km encountered over their lifetime. The size of the radius along the trajectory is given by the color bar (in km).

Considering now the cyclonic versus anticyclonic patterns, W13Q cyclonic eddies are dominant for all radius classes, except for the smallest ones (~10 km) (Figure 10b). Nevertheless, as previously mentioned, the generated anticyclonic structures are more unstable and form small structures with short lifetime (shorter than a week).

Focusing on these small eddies of interest, we further investigate trajectories of eddies with a maximum radius between 20 and 30 km, which represents about 50% of the eddies (Figure 10a). As presented in Figure 10b, anticyclonic eddies are less numerous than cyclonic ones for this radius range (Figures 11a versus 11b, respectively). Furthermore, the anticyclonic eddy trajectories are shorter than the cyclonic ones (Figure 11b) because of the centrifugal instability that weakens anticyclonic eddies (Dong et al., 2007). While Calil et al. (2008) showed that cyclonic (anticyclonic) eddies tend to propagate poleward (equatorward) in the Hawaiian archipelago, trajectories of eddies generated leeward the Marquesas Islands are mostly zonal and do not present such a meridian trend. Indeed, while 61% (54.8%) of the cyclonic (anticyclonic) eddies propagate equatorward (southward), their meridian mean latitude change is only of 0.0163° (0.0182°). This might be explained by the lower latitude of the Marquesas archipelago inducing a weaker beta effect than in Hawaii.

### 3.5. An Insight to a Possible Eddy Induced Biological Activity

Hasegawa et al. (2009) hypothesized that a combination of three processes can enrich the surface layer in island wakes: the propagation of coastal rich waters formed in the lee of the islands by eddy shedding, the vertical advection of the Deep Chlorophyll Maximum (DCM) toward the surface in the island wake, and the uplift of nutrient-rich deep waters by the strongest cyclonic eddies. We show that, when the SEC encounters the Marquesas Islands, it generates eddies in the lee of the archipelago (Figure 9a). These eddies can trap and propagate inshore waters in the island wake. Thus, if these inshore waters have been previously enriched in proximity of the islands, the biological activity can be enhanced. An increase of the sea surface concentration of chlorophyll in the lee of an island could also be induced by the vertical advection of the DCM. During the "Pakaihi i te Moana" expedition, a correlation between the depth of the DCM and the mixed layer depth (MLD) has been reported in the archipelago (Martinez et al., 2016). On average, the DCM is deeper (shallower) in the northern (southern) region of the archipelago consistently with the MLD (60 m versus 30 m). Our results show strong vertical velocities at the MLD associated with the eddies of the island wake (Figure 12). This high vertical activity might induce the vertical advection of the DCM toward the surface. The evaluation of the impact of the fine-scale dynamics on the nutricline is beyond the scope of the present study and will need further research. Indeed, to assess the uplift of
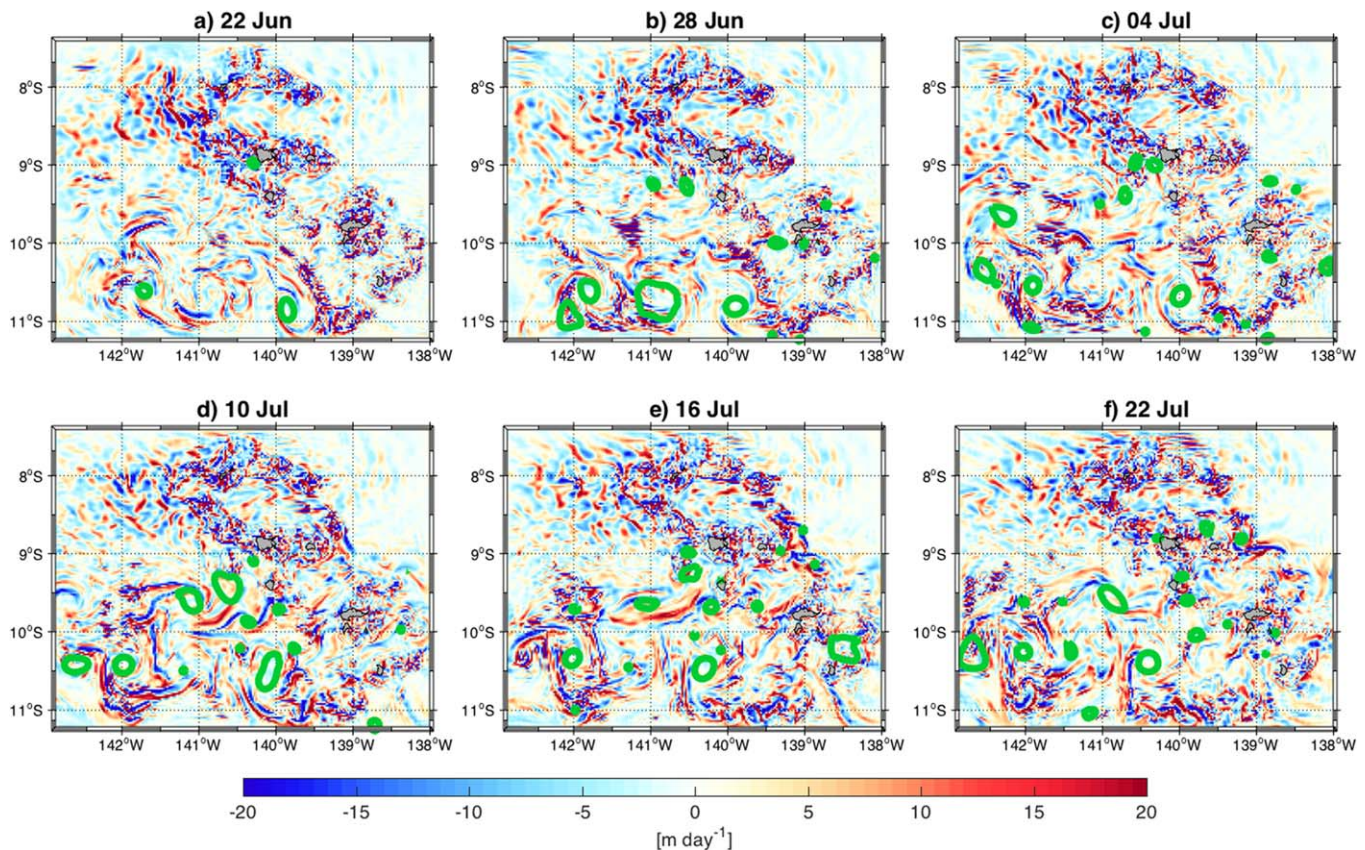
**Figure 12.** Snapshots of vertical velocities (in m d$^{-1}$) as in Figure 8, but at the mixed layer depth.

nutrient-rich deep waters by cyclonic eddies and the associated biological activity, a coupled physical-biogeochemical model is required.

## 4. Conclusions and Perspectives

The island wake in the Marquesas archipelago has been characterized in the present study, providing new insights into the spatial and seasonal variability of the fine-scale dynamics of this oceanic region. We based our analysis on the ocean circulation model ROMS-AGRIF with a 1/45° child grid resolution and forced by climatological mean fields. The high spatial and temporal resolution allows characterizing warm SST patterns just behind the Marquesas Islands. These patterns likely due to shadow zones of weak currents have been consistently observed leeward several islands (Barton, 2001; Caldeira et al., 2002; Chavanne et al., 2002).

Accordingly to a rough approximation of the local Reynolds number, only Nuku Hiva, the biggest island of the archipelago, would be expected to generate a wake of propagating eddies. However, the mean *EKE* and the use of an automated eddy detection algorithm reveals that eddy generation also occurs leeward the other islands, inshore and offshore. The energy budget analysis reveals that eddies are generated by a combination of wind power input, barotropic and baroclinic energy conversion. These generated eddies are cyclonic dominant due to the small size of the islands in comparison to the Rossby radius. Most of the eddies have their maximum radius between 20 and 30 km.

Our physical model results provide insight to explain the Marquesas biological enhancement. We suggest that the combination of at least two of the three processes proposed by Hasegawa et al. (2009) enriches surface layers via eddy activity: the propagation of rich waters formed in the lee of the islands by eddy shedding and the vertical advection of the DCM toward the surface in the island wake. To further investigate the third process, i.e. the possibility of an uplift of nutrient-rich waters by the cyclonic eddies, new in situ data, and the use of a coupled physical-biogeochemical numerical model are required.

## References

Alaee, M. J., Ivey, G., & Pattiaratchi, C. (2004). Secondary circulation induced by flow curvature and Coriolis effects around headlands and islands. *Ocean Dynamics*, *54*(1), 27–38. https://doi.org/10.1007/s10236-003-0058-3

Amores, A., Monserrat, S., & Marcos, M. (2013). Vertical structure and temporal evolution of an anticyclonic eddy in the Balearic Sea (western Mediterranean). *Journal of Geophysical Research: Oceans*, *118*, 2097–2106. https://doi.org/10.1002/jgrc.20150

Andrade, I., Sangrà, P., Hormazabal, S., & Correa-Ramirez, M. (2014). Island mass effect in the Juan Fernández Archipelago (33°S), Southeastern Pacific. *Deep Sea Research, Part I*, *84*, 86–99. https://doi.org/10.1016/j.dsr.2013.10.009

Auad, G., Pares-Sierra, A., & Vallis, G. K. (1991). Circulation and energetics of a model of the California Current system.pdf. *Journal of Physical Oceanography*, *21*(10), 1534–1552.

Barton, E. D. (2001). Island wakes. In J. H. Steele, (Ed.), *Encyclopedia of ocean sciences* (Vol. 3, pp. 1397–1403). Oxford, UK: Academic Press. https://doi.org/10.1006/rwos.2001.0140

Beckmann, A., & Haidvogel, D. B. (1993). Numerical simulation of flow around a tall isolated seamount. Part I: Problem formulation and model accuracy. *Journal of Physical Oceanography*, *23*(8), 1736–1753. https://doi.org/10.1175/1520-0485(1993)023<1736:NSOFAA>2.0.CO;2

Bonjean, F., & Lagerloef, G. S. E. (2002). Diagnostic model and analysis of the surface currents in the tropical Pacific Ocean. *Journal of Physical Oceanography*, *32*(10), 2938–2954. https://doi.org/10.1175/1520-0485(2002)032<2938:DMAAOT>2.0.CO;2

Caldeira, R. M. A., Groom, S., Miller, P., Pilgrim, D., & Nezlin, N. P. (2002). Sea-surface signatures of the island mass effect phenomena around Madeira Island, Northeast Atlantic. *Remote Sensing of Environment*, *80*(2), 336–360. https://doi.org/10.1016/S0034-4257(01)00316-9

Caldeira, R. M. A., & Marchesiello, P. (2002). Ocean response to wind sheltering in the Southern California Bight. *Geophysical Research Letters*, *29*(13), 1635. https://doi.org/10.1029/2001GL014563

Calil, P. H. R., Richards, K. J., Jia, Y., & Bidigare, R. R. (2008). Eddy activity in the lee of the Hawaiian Islands. *Deep Sea Research, Part II*, *55*(10–13), 1179–1194. https://doi.org/10.1016/j.dsr2.2008.01.008

Chang, M. H., Tang, T. Y., Ho, C. R., & Chao, S. Y. (2013). Kuroshio-induced wake in the lee of Green Island off Taiwan. *Journal of Geophysical Research: Oceans*, *118*, 1508–1519. https://doi.org/10.1002/jgrc.20151

Chavanne, C., Flament, P., Lumpkin, R., Dousset, B., & Bentamy, A. (2002). Scatterometer observations of wind variations induced by oceanic islands: Implications for wind-driven ocean circulation. *Canadian Journal of Remote Sensing*, *28*(3), 466–474. https://doi.org/10.5589/m02-047

Chelton, D. B., deSzoeke, R. A., Schlax, M. G., El Naggar, K., & Siwertz, N. (1998). Geographical variability of the first baroclinic Rossby radius of deformation. *Journal of Physical Oceanography*, *28*(3), 433–460. https://doi.org/10.1175/1520-0485(1998)028<0433:GVOTFB>2.0.CO;2

Chen, R., Thompson, A. F., & Flierl, G. R. (2016). Time-dependent eddy-mean energy diagrams and their application to the ocean. *Journal of Physical Oceanography*, *46*(9), 2827–2850. https://doi.org/10.1175/JPO-D-16-0012.1

Cummings, J. A., & Smedstad, O. M. (2013). Variational data assimilation for the global ocean. In *Data assimilation for atmospheric, oceanic and hydrologic applications* (Vol. II, pp. 303–343). Berlin, Heidelberg: Springer.

da Silva, A. M., Young, C. C., & Levitus, S. (1994). *Atlas of surface marine data 1994. Volume 4: Anomalies of fresh water fluxes*, NOAA ATLAS NESDIS 9, 308 p.). Sliver Spring, MD: NOAA.

Debreu, L., & Blayo, E. (2008). Two-way embedding algorithms: A review. *Ocean Dynamics*, *58*(5–6), 415–428. https://doi.org/10.1007/s10236-008-0150-9

Debreu, L., Marchesiello, P., Penven, P., & Cambon, G. (2012). Two-way nesting in split-explicit ocean models: Algorithms, implementation and validation. *Ocean Modelling*, *49–50*, 1–21. https://doi.org/10.1016/j.ocemod.2012.03.003

Dietrich, D., Bowman, M., & Lin, C. (1996). Numerical studies of small island wakes in the ocean. *Geophysical & Astrophysical Fluid Dynamics*, *83*(3–4), 195–231. https://doi.org/10.1080/03091929608208966

DiGiacomo, P. M., & Holt, B. (2001). Satellite observations of small coastal ocean eddies in the Southern California Bight. *Journal of Geophysical Research*, *106*(10), 22521–22543. https://doi.org/10.1029/2000JC000728

Doglioli, A. M., Blanke, B., Speich, S., & Lapeyre, G. (2007). Tracking coherent structures in a regional ocean model with wavelet analysis: Application to Cape Basin eddies. *Journal of Geophysical Research*, *112*, C05043. https://doi.org/10.1029/2006JC003952

Dong, C., Lin, X., Liu, Y., Nencioli, F., Chao, Y., Guan, Y., et al. (2012). Three-dimensional oceanic eddy analysis in the Southern California Bight from a numerical product. *Journal of Geophysical Research: Oceans*, *117*, C00H14. https://doi.org/10.1029/2011JC007354

Dong, C., McWilliams, J. C., & Shchepetkin, A. F. (2007). Island wakes in deep water. *Journal of Physical Oceanography*, *37*(4), 962–981. https://doi.org/10.1175/JPO3047.1

Doty, M. S., & Oguri, M. (1956). The island mass effect. *Journal du Conseil*, *22*(1), 33–37. https://doi.org/10.1093/icesjms/22.1.33

Emery, W. J. (2001). Water types and water masses. In J. H. Steele, (Ed.), *Encyclopedia of ocean sciences* (Vol. 6, pp. 3179–3187). Oxford, UK: Academic Press. https://doi.org/10.1006/rwos.2001.0108

Gaillard, F., Reynaud, T., Thierry, V., Kolodziejczyk, N., & Von Schuckmann, K. (2016). In situ-based reanalysis of the global ocean temperature and salinity with ISAS: Variability of the heat content and steric height. *Journal of Climate*, *29*(4), 1305–1323. https://doi.org/10.1175/JCLI-D-15-0028.1

Halo, I., Penven, P., Backeberg, B., Ansorge, I., Shillington, F., & Roman, R. (2014). Mesoscale eddy variability in the southern extension of the East Madagascar Current: Seasonal cycle, energy conversion terms, and eddymean properties. *Journal of Geophysical Research: Oceans*, *119*, 7324–7356. https://doi.org/10.1002/2014JC009820

Harrison, D. E., & Robinson, A. R. (1978). Energy analysis of open regions of turbulent flows - mean eddy energetics of a numerical ocean circulation experiment. *Dynamics of Atmospheres and Oceans*, *2*(2), 185–211. https://doi.org/10.1016/0377-0265(78)90009-X

Hasegawa, D., Lewis, M. R., & Gangopadhyay, A. (2009). How islands cause phytoplankton to bloom in their wakes. *Geophysical Research Letters*, *36*, L20605. https://doi.org/10.1029/2009GL039743

Hasegawa, D., Yamazaki, H., Lueck, R. G., & Seuront, L. (2004). How islands stir and fertilize the upper ocean. *Geophysical Research Letters*, *31*, L16303. https://doi.org/10.1029/2004GL020143

Hasegawa, D., Yamazaki, H., Ishimaru, T., Nagashima, H., & Koike, Y. (2008). Apparent phytoplankton bloom due to island mass effect. *Journal of Marine Systems*, *69*(3–4), 238–246. https://doi.org/10.1016/j.jmarsys.2006.04.019

Heywood, K. J., Barton, E. D., & Simpson, J. H. (1990). The effects of flow disturbance by an oceanic island. *Journal of Marine Research*, *48*, 55–73. https://doi.org/10.1357/002224090784984623

Heywood, K. J., Stevens, D. P., & Bigg, G. R. (1996). Eddy formation behind the tropical island of Aldabra. *Deep Sea Research, Part I*, *43*(4), 555–578. https://doi.org/10.1016/0967-0637(96)00097-0

Hristova, H. G., Kessler, W. S., McWilliams, J. C., & Molemaker, M. J. (2014). Mesoscale variability and its seasonality in the Solomon and Coral Seas. *Journal of Geophysical Research: Oceans*, *119*, 4669–4687. https://doi.org/10.1002/2013JC009741

Jiménez, B., Sangrà, P., & Mason, E. (2008). A numerical study of the relative importance of wind and topographic forcing on oceanic eddy shedding by tall, deep water islands. *Ocean Modelling*, *22*(3–4), 146–157. https://doi.org/10.1016/j.ocemod.2008.02.004

Kang, D., & Curchitser, E. N. (2015). Energetics of eddy-mean flow interactions in the Gulf Stream region. *Journal of Physical Oceanography*, *45*, 1103–1120. https://doi.org/10.1175/JPO-D-14-0200.1

Karnauskas, K. B., Johnson, G. C., & Murtugudde, R. (2017). On the climate impacts of atolls in the central equatorial Pacific. *International Journal of Climatology*, *37*(1), 197–203. https://doi.org/10.1002/joc.4697

Kersalé, M., Doglioli, A. M., & Petrenko, AA. (2011). Sensitivity study of the generation of mesoscale eddies in a numerical model of Hawaii islands. *Ocean Science*, *7*(3), 277–291. https://doi.org/10.5194/os-7-277-2011

Large, W. G., McWilliams, J. C., & Doney, S. C. (1994). Oceanic vertical mixing: A review and a model with a nonlocal boundary layer parameterization. *Reviews of Geophysics*, *32*(4), 363–403. https://doi.org/10.1029/94RG01872

Legeckis, R., Brown, C. W., Bonjean, F., & Johnson, E. S. (2004). The influence of tropical instability waves on phytoplankton blooms in the wake of the Marquesas Islands during 1998 and on the currents observed during the drift of the Kon-Tiki in 1947. *Geophysical Research Letters*, *31*, L23307. https://doi.org/10.1029/2004GL021637

Liang, J. H., McWilliams, J. C., Kurian, J., Colas, F., Wang, P., & Uchiyama, Y. (2012). Mesoscale variability in the northeastern tropical Pacific: Forcing mechanisms and eddy properties. *Journal of Geophysical Research: Oceans*, *117*, C07003. https://doi.org/10.1029/2012JC008008

Liu, Y., Dong, C., Guan, Y., Chen, D., McWilliams, J., & Nencioli, F. (2012). Eddy analysis in the subtropical zonal band of the North Pacific Ocean. *Deep Sea Research, Part I*, *68*, 54–67. https://doi.org/10.1016/j.dsr.2012.06.001

Locarnini, R. A., Mishonov, A. V., Antonov, J. I., Boyer, T. P., Garcia, H. E., Baranova, O. K., et al. (2013). *World Ocean Atlas 2013. Vol. 1: Temperature, S. Levitus, Ed.; A. Mishonov, Tech. Ed.* (NOAA Atlas NESDIS *73*, 40 p.). Sliver Spring, MD: NOAA. https://doi.org/10.1182/blood-2011-06-357442

Lungu, T., & Callahan, P. S. (2006). *QuikSCAT science data product user's manual: Overview and geophysical data products* (D-18053-Rev A, version 3, 91 p). Pasadena, CA: Jet Propulsion Laboratory, California Institute of Technology.

Marchesiello, P., McWilliams, J. C., & Shchepetkin, A. (2001). Open boundary conditions for long-term integration of regional oceanic models. *Ocean Modelling*, *3*(1–2), 1–20. https://doi.org/10.1016/S1463-5003(00)00013-5

Marchesiello, P., McWilliams, J. C., Shchepetkin, A., Physics, P., & Angeles, L. (2003). Equilibrium structure and dynamics of the California current system. *Journal of Physical Oceanography*, *33*(4), 753–783. https://doi.org/10.1175/1520-0485(2003)33<753:ESADOT>2.0.CO;2

Martinez, E., Ganachaud, A., Lefevre, J., & Maamaatuaiahutapu, K. (2009). Central South Pacific thermocline water circulation from a high-resolution ocean model validated against satellite data: Seasonal variability and El Niño 1997–1998 influence. *Journal of Geophysical Research*, *114*, C05012. https://doi.org/10.1029/2008JC004824

Martinez, E., & Maamaatuaiahutapu, K. (2004). Island mass effect in the Marquesas Islands: Time variation. *Geophysical Research Letters*, *31*, L18307. https://doi.org/10.1029/2004GL020682

Martinez, E., Rodier, M., & Maamaatuaiahutapu, K. (2016). Environnement océanique des Marquises. In R. Galzin, S. D. Duron, & J. Y. Meyer (Eds.), *Biodiversité terrestre et marine des îles Marquises* (pp. 123–136). Paris, France: Société Française d'Ichtyologie.

Maury, R. C., Guille, G., Hervé, G., Catherine, C., Legendre, C., Rossi, P., et al. (2014). Géologie des Marquises: des volcans boucliers intra-océaniques effondrés issus d'un point chaud atypique Géologie des Marquises: des volcans boucliers intra-océaniques effondrés issus d' un point chaud atypique. *Geology of France*, *1*(8), 111–135.

Mkhinini, N., Coimbra, A. L. S., Stegner, A., Arsouze, T., Taupier-Letage, I., & Béranger, K. (2014). Long-lived mesoscale eddies in the eastern Mediterranean Sea: Analysis of 20 years of AVISO geostrophic velocities. *Journal of Geophysical Research: Oceans*, *119*, 8603–8626. https://doi.org/10.1002/2014JC010176

Neill, S. P., & Elliott, A. J. (2004). Observations and simulations of an unsteady island wake in the Firth of Forth, Scotland. *Ocean Dynamics*, *54*(3–4), 324–332. https://doi.org/10.1007/s10236-003-0084-1

Nencioli, F., Dong, C., Dickey, T., Washburn, L., & Mcwilliams, J. C. (2010). A vector geometry-based eddy detection algorithm and its application to a high-resolution numerical model product and high-frequency radar surface velocities in the Southern California Bight. *Journal of Atmospheric and Oceanic Technology*, *27*(3), 564–579. https://doi.org/10.1175/2009JTECHO725.1

O'Connor, B. M., Fine, R. A., & Olson, D. B. (2005). A global comparison of subtropical underwater formation rates. *Deep Sea Research, Part I*, *52*(9), 1569–1590. https://doi.org/10.1016/j.dsr.2005.01.011

Palacios, D. M. (2002). Factors influencing the island-mass effect of the Galápagos Archipelago. *Geophysical Research Letters*, *29*(23), 2134. https://doi.org/10.1029/2002GL016232

Penven, P., Marchesiello, P., Debreu, L., & Lefèvre, J. (2007). Software tools for pre- and post-processing of oceanic regional simulations. *Environmental Modelling & Software*, *23*(5), 660–662. https://doi.org/10.1016/j.envsoft.2007.07.004

Qiu, B., & Chen, S. (2004). Seasonal modulations in the Eddy Field of the South Pacific Ocean. *Journal of Physical Oceanography*, *34*(7), 1515–1527. https://doi.org/10.1175/1520-0485(2004)034<1515:SMITEF>2.0.CO;2

Sangrà, P., Basterretxea, G., Pelegrí, J. L., & Arístegui, J. (2001). Chlorophyll increase due to internal waves on the shelf break of Gran Canaria (Canary Islands). *Signals*, *65*, 89–97. https://doi.org/10.3989/scimar.2001.65s189

Sangrà, P., Pelegrí, J. L., Hernández-Guerra, A., Arregui, I., Martín, J. M., Marrero-Díaz, A., et al. (2005). Life history of an anticyclonic eddy. *Journal of Geophysical Research*, *110*, C03021. https://doi.org/10.1029/2004JC002526

Shchepetkin, A. F., & McWilliams, J. C. (2003). A method for computing horizontal pressure-gradient force in an oceanic model with non-aligned vertical coordinate. *Journal of Geophysical Research*, *108*(C3), 3090. https://doi.org/10.1029/2001JC001047

Shchepetkin, A. F., & McWilliams, J. C. (2005). The regional oceanic modeling system ({ROMS}): A split-explicit, free-surface, topography-following-coordinate oceanic model. *Ocean Modelling*, *9*, 347–404. https://doi.org/10.1016/j.ocemod.2004.08.002

Signorini, S. R., McClain, C. R., & Dandonneau, Y. (1999). Mixing and phytoplankton bloom in the wake of the Marquesas Islands. *Geophysical Research Letters*, *26*(20), 3121–3124. https://doi.org/10.1029/1999GL010470

Smith, W. H., & Sandwell, D. (1997). Global sea floor topography from satellite altimetry and ship depth soundings. *Science*, *277*(5334), 1956–1962. https://doi.org/10.1126/science.277.5334.1956

Stegner, A. (2014). Oceanic Island wake flows in the laboratory. In T. von Larcher & P. D. Williams (Eds.), *Modeling atmospheric and oceanic flows: Insights from laboratory experiments and numerical simulations* (pp. 265–276). Hoboken, NJ: John Wiley & Sons, Inc.

Sun, Z., Zhang, Z., Zhao, W., & Tian, J. (2016). Interannual modulation of eddy kinetic energy in the northeastern South China Sea as revealed by an eddy-resolving OGCM. *Journal of Geophysical Research: Oceans*, *121*, 3190–3201. https://doi.org/10.1002/2015JC011497

Tomczak, M. (1988). Island wakes in deep and shallow water. *Journal of Geophysical Research*, *93*(8), 5153–5154.

Wolanksi, E., Asaeda, T., Tanaka, A., & Deleersnijder, E. (1996). Three-dimensional island wakes in the field, laboratory experiments and numerical models. *Continental Shelf Research*, *16*(11), 1437–1452. https://doi.org/10.1016/0278-4343(95)00087-9

Wyrtki, K. (1981). An estimate of equatorial upwelling in the Pacific. *Journal of Physical Oceanography*, *11*, 1205–1214.

Xu, Y., & Scott, R. B. (2008). Subtleties in forcing eddy resolving ocean models with satellite wind data. *Ocean Modelling*, *20*(3), 240–251. https://doi.org/10.1016/j.ocemod.2007.09.003

Yan, X., Ho, C., Zheng, Q., & Klemas, V. (1992). Temperature and size variabilities of the Western Pacific warm pool. *Science*, *258*(5088), 1643–1645.

Zweng, M. M., Reagan, J. R., Antonov, J. I., Mishonov, A. V., Boyer, T. P., Garcia, H. E., et al. (2013). World Ocean Atlas 2013, Volume 2: Salinity. *NOAA Atlas NESDIS*, *119*(1), 227–237. https://doi.org/10.1182/blood-2011-06-357442